

SPHEREx Pre-Perihelion Mapping of H₂O, CO₂, and CO in Interstellar Object 3I/ATLAS

CAREY M. LISSE,^{1,2} YOONSOO P. BACH,³ BRENDAN P. CRILL,^{4,5} PHIL M. KORNGUT,⁵ ARI J. CUKIERMAN,⁵
SEAN A. BRYAN,⁶ ASANTHA COORAY,⁷ C. DARREN DOWELL,^{4,5} MICHAEL W. WERNER,⁴ JOSEPH L. HORA,⁸
ZAFAR RUSTAMKULOV,⁹ JEONG-EUN LEE,¹⁰ BUMHOO LIM,^{10,11} Y. R. FERNANDEZ,¹² VOLKER TOLLS,⁸ W. T. REACH,¹³
O. DORÉ,^{4,5} MICHAEL ZEMCOV,^{14,4} JAMES J. BOCK,^{5,4} YUN-TING CHENG,^{5,4} C. CHAMPAGNE,¹⁵ SEUNGWON CHOI,^{10,11}
M. CONNELLEY,¹⁶ J. P. EMERY,¹⁵ SPENCER EVERETT,⁵ ANDREAS L. FAISST,⁹ JOOYEON GEEM,¹⁷ HOWARD HUI,⁵
MASATERU ISHIGURO,^{10,11} SUNHO JIN,³ HANGBIN JO,^{10,11} MAX MAHLKE,¹⁸ DANIEL C. MASTERS,⁹ GARY J. MELNICK,⁸
CHI H. NGUYEN,⁵ ROBERTA PALADINI,⁹ M. L. SITKO,¹³ AND YUJIN YANG³

¹Johns Hopkins University, 3400 N Charles St, Baltimore, MD 21218, USA

²Johns Hopkins University Applied Physics Laboratory, Laurel, MD 20723, USA

³Korea Astronomy and Space Science Institute (KASI), 776 Daedeok-daero, Yuseong-gu, Daejeon 34055, Republic of Korea

⁴Jet Propulsion Laboratory, California Institute of Technology, 4800 Oak Grove Drive, Pasadena, CA 91109, USA

⁵Department of Physics, California Institute of Technology, 1200 E. California Boulevard, Pasadena, CA 91125, USA

⁶School of Earth and Space Exploration, Arizona State University, 781 Terrace Mall, Tempe, AZ 85287 USA

⁷Department of Physics & Astronomy, University of California Irvine, Irvine CA 92697, USA

⁸Center for Astrophysics | Harvard & Smithsonian, Optical and Infrared Astronomy Division, Cambridge, MA 02138, USA

⁹IPAC, California Institute of Technology, MC 100-22, 1200 E California Blvd Pasadena, CA 91125, USA

¹⁰Department of Physics and Astronomy, Seoul National University, 1 Gwanak-ro, Gwanak-gu, Seoul 08826, Republic of Korea

¹¹SNU Astronomy Research Center, Department of Physics and Astronomy, Seoul National University, Gwanak-ro 1, Gwanak-gu, Seoul 08826, Republic of Korea

¹²Department of Physics, University of Central Florida, Orlando, FL 32816-2385, USA

¹³Space Science Institute, 4765 Walnut Street, Suite B, Boulder, CO 80301, USA

¹⁴School of Physics and Astronomy, Rochester Institute of Technology, 1 Lomb Memorial Dr., Rochester, NY 14623, USA

¹⁵Northern Arizona University, Department of Astronomy and Planetary Science, Flagstaff, AZ, USA

¹⁶University of Hawaii, 640 N. Aohoku Place, Hilo, HI 96720, USA

¹⁷Asteroid Engineering Laboratory, Luleå University of Technology, Box 848, Kiruna, 98128, Sweden

¹⁸Universit'e Marie et Louis Pasteur, CNRS, Institut UTINAM (UMR 6213), 'equipe Astro, F-25000 Besan,con, France

ABSTRACT

From 01- to 15-Aug-2025UT, the SPHEREx spacecraft observed interstellar object 3I/ATLAS. Using $R = 40\text{--}130$ spectrophotometry at $\lambda = 0.7\text{--}5\ \mu\text{m}$, light curves, spectra, and imaging of 3I were obtained. From these, robust detections of water gas emission at $2.7\text{--}2.8\ \mu\text{m}$ and CO₂ gas at $4.23\text{--}4.27\ \mu\text{m}$ plus tentative detections of ¹³CO₂ and CO gas were found. A slightly extended H₂O coma was detected, and a huge CO₂ atmosphere of extending out to at least 4.2×10^5 km was discovered. Gas production rates and 1σ errors for H₂O, ¹²CO₂, ¹³CO₂, and CO were $Q_{gas} = 3.2 \times 10^{26} \pm 20\%$, $1.6 \times 10^{27} \pm 10\%$, $1.3 \times 10^{25} \pm 25\%$, and $1.0 \times 10^{26} \pm 25\%$, respectively. Co-addition of all $\lambda = 1.0\text{--}1.5\ \mu\text{m}$ scattered light continuum images from produced a high SNR image consistent with an unresolved source. The scattered light lightcurve showed $\lesssim 15\%$ variability over the observation period. The absolute brightness of 3I at $1.0\text{--}1.5\ \mu\text{m}$ is consistent with a < 2.5 km radius nucleus surrounded by a 100 times brighter coma. The $1.5\text{--}4.0\ \mu\text{m}$ continuum structure shows a strong feature commensurate with water ice absorption seen in KBOs and distant comets. The observed cometary behavior of 3I, including its preponderance of CO₂ emission, lack of CO output, small size, and predominance of large icy chunks of material in a flux-dominant coma is similar to the behavior of short period comet 103P/Hartley 2, the "hyperactive comet" flyby target of the NASA Deep Impact extended mission in 2010. This correspondence suggests that ISOs can be significantly thermally processed before ejection into the ISM, and by comparison to 1I and 2I, can be widely variable in their physical outcome.

Keywords: Galaxies (573) — Cosmology (343) — High Energy astrophysics (739) — Interstellar medium (847) — Stellar astronomy (1583) — Solar physics (1476)

1. INTRODUCTION

SPHEREx (Spectro-Photometer for the History of the Universe, Epoch of Reionization and Ices Explorer) is a new NASA mission launched into low-Earth, Sun-synchronous orbit (altitude ≈ 675 km) on 11-Mar-2025 UT (Doré et al. 2016, 2018; Bock et al. 2025). Conducting a 102-band near-infrared spectrophotometric survey of the entire sky over the course of 2 years, it was designed primarily to study (1) inflationary cosmology, (2) the history of galaxy formation, and (3) the abundance of astrobiologically important molecular ices in planet-forming regions. SPHEREx will observe and catalog measurements of everything along a line of sight on the sky—from local solar system objects (asteroids, comets, planets, KBOs) to main sequence stars, to distant quasars. One of these objects, 3I/ATLAS (3I, hereafter), was recently discovered on 01-Jul-2025 (Denneau et al. 2025) and verified within the next few days as only the 3rd ever macroscopic body detected hurtling through the solar system from the depths of interstellar space. Termed “ISOs”, bodies like 3I represent unique samples of exosystem material delivered close to Earth “for free”, allowing in-depth remote sensing analysis of their size, shape, composition, and temporal behavior during the few months when they are passing through the inner solar system.

Analysis of 3I’s orbit and apparent motion on the sky [JPL Horizons Ref] with respect to the SPHEREx sky survey region (Solar elongation $\sim 90^\circ$; Bryan et al. (2025)) showed that the object would be visited ~ 70 times from 08- to 15-Aug-2025 during the normal survey (Fig. 1), with some gaps in wavelength coverage, especially around $3\ \mu\text{m}$, due to 3I’s rapid apparent sky motion. The project then proceeded to design, test, and implement a special observing mode, only 2 months after the start of the mission’s all-sky survey, to augment the total number of visits to 3I up to 160 flux measurements while completely characterizing the object from $0.75\text{--}5.0\ \mu\text{m}$.

The initial results from the first ~ 70 SPHEREx normal survey visits to 3I, as published in Lisse et al. (2025), resulted in the discovery of a giant CO_2 coma surrounding the nucleus and the presence of large ($> 100\ \mu\text{m}$) water-ice rich grains in the coma. Scattered light was detected from the nucleus and coma grains at $\lambda \lesssim 2.3\ \mu\text{m}$, but only $3\text{-}\sigma$ upper limits were placed on the emission rates of H_2O and CO gas.

In this paper, with more than double the total measurements and a much better data reduction and data calibration, we extend the preliminary SPHEREx discoveries to include a robust detection of the water gas emission feature at $2.7\text{--}2.8\ \mu\text{m}$ and a marginal detection of CO gas emission at $4.7\ \mu\text{m}$.

In addition, the detected $^{12}\text{CO}_2$ line emission at $4.25\text{--}4.27\ \mu\text{m}$ was so strong that we searched for substructure in it. While we were not able to resolve the 4.25 vs $4.27\ \mu\text{m}$ doublet at the peak, we were able to spectrally distinguish a shoulder at $4.37\ \mu\text{m}$ where emission due to $^{13}\text{CO}_2$ is found. Assuming the same distribution pattern as for the $^{12}\text{CO}_2$ and thus the same aperture size, we find the abundance ratio of $^{13}\text{CO}_2$ to $^{12}\text{CO}_2$ to be the same, within the error bars of the measurement, as reported by Cordiner et al. (2025) using JWST NIRSPEC IFU spectroscopy.

SPHEREx’s unique observational strengths lie in its ability to spectrophotometrically image an object at $0.75\text{--}5.0\ \mu\text{m}$ over many weeks and on large angular scales. SPHEREx’s spectrophotometric quality is attested to by its overall excellent 3I spectral match to the published $0.7\text{--}5.3\ \mu\text{m}$ JWST spectrum (Cordiner et al. 2025); where they differ, in the gas emission lines, it is always SPHEREx’s measurement that is the larger due to its much larger projected observing aperture (Fig. 2). (It is important to note that the area of the SPHEREx central pixel is 4 times the area of the entire JWST NIRSPEC IFU field of view.) SPHEREx’s temporal capabilities are demonstrated by the 12 day long dust continuum reflectance lightcurve (Fig. 1c) and its large field image quality by $\sim 6'$ wide CO_2 coma detection shown in Fig. 3.

The chief systematic found for the SPHEREx 3I observations is confusion with background stars. Other effects, like motion with respect to the Sun and Earth, and changes in phase angle, were small and easily corrected for. Object variability, which can introduce large uncertainties in SPHEREx spectrophotometry obtained piecemeal over 15 days, was not an issue due to the lack of any observed lightcurve variation greater than 15% found (Fig. 1c) and in reports by other groups (Kareta et al. 2025; Chandler et al. 2025). This lack of variation, in turn, is likely due to the dominance of the observed flux by the slowly time-varying smooth coma, which can mask any rapid projected surface area variations of an asymmetric rotating nucleus.

In this Letter we describe the complete set of August 2025 SPHEREx observations of 3I, and their data quality, reduction, and analysis. Because of these observations, we now understand that the extended optical morphology seen for 3I since its discovery is the product of robust CO₂ gas sublimation that was undetectable in the first UVIS characterizations of the object reported in July 2025. We also find a very CO-poor but H₂O-ice rich cometary object with its water gas production just beginning to turn on, and evidence for thermal processing of the body as seen in highly thermalized inner solar system comets. We find good concordance with other August 2025 imaging and spectroscopic measures of the object. We use these findings to argue that the surface layers of 3I must have been well-thermally processed before its ejection from its home system into the ISM, and that such thermal processing happens more rapidly than exosystems dynamically relax.

2. OBSERVATIONS

SPHEREx obtained 160 frames with 3I within the field of view from 2025-08-01 UT 08:01:07 to 2025-08-15 UT 12:43:48 (midpoints of exposures), including 94 exposures produced by deliberately adjusting the survey planning algorithm to place 3I in the FoV. A subset of these were downlinked and processed promptly, leading to our express publication in Lisse et al. (2025). In this work, we analyze all 160 frames (Table 1). The orbital geometry of the observation and the sky mosaic images are shown in Fig. 1.

Ancillary lightcurve observations were obtained using the remote/robotic Solar system Objects Lightcurve Observatory (SOLO; B. Lim et al., submitted to JKAS), a Celestron LLC’s RASA11 telescope¹⁹ located at Sierra Remote Observatory²⁰, CA, USA in order to independently check the SPHEREx time domain trending. Combined with the currently installed imaging sensor at the prime focus, KL4040²¹, and a UV-cut clear filter, the total throughput of the SOLO system as of writing is effectively sensitive to $\sim 0.4\text{--}1.0\ \mu\text{m}$, with a response closely comparable to the Gaia G band. The results are shown in Fig. 1c, and are consistent with the low (if any) level of variability detected by SPHEREx.

Ancillary spectral observations were used to independently check the SPHEREx spectral measurements were obtained at the NASA Infrared Telescope Facility (IRTF) on the nights of 09 and 10-Aug-2025 using the

SpeX instrument in $R \sim 50$, $\lambda = 0.7\text{--}2.5\ \mu\text{m}$ prism spectroscopy mode (Fig. 2). These measurements were vital for verifying initial SPHEREx spectrophotometric data reductions and quickly bootstrapping early photometric measures, and the two sets of measurements were found to be closely consistent, especially the strong dropoff past $2.3\ \mu\text{m}$ in the IRTF spectrum that was initially believed to be an instrumental artifact near the end of the spectral order.

3. DATA REDUCTION

We first simulated the exposures using the SPHEREx reference catalog (Y. Yang et al., in prep.) and the SPHEREx Sky Simulator (Crill et al. 2025). The simulated images, which do not have 3I in them, were then subtracted from the calibrated raw Level 2b (l2b) image data provided by the SPHEREx science pipeline in Quick Release 2 (QR2; SPHEREx Explanatory Supplement). This was extremely helpful in removing the estimated flux of field objects within 3I’s aperture, flagging less reliable images and extendedness artifacts, and significantly improved the final spectrum.

For signal extraction, we applied simple circular aperture photometry with a $12''$ radius (~ 2 pixels, depending on the location in the FoV due to the distortion). The residual local sky background was estimated from a circular annulus with inner and outer radii of $\approx 1'$ and $3'$, respectively. The photometry at the same celestial location from the original l2b image, simulated image, and the simulation-subtracted image are F_{2b} , F_{sim} , and $F_{\lambda} = F_{2b} - F_{\text{sim}}$, respectively.

We verified that the results are robust against variations in the annulus size and different sky estimation algorithms. As an additional *null test*, we measured the single pixel value minus the estimated sky from the surrounding annulus for several pixels that are neither flagged as bad nor expected to contain source signals (based on the reference catalog) within each image. These values are consistent with zero, with scatter comparable to the expected pixel variance. This confirms that the sky estimation is reliable at the pixel-variance level.

The uncertainty of F_{λ} , dF_{λ} , is obtained based on the aperture sum of the associated variance map of the l2b image, quadratically combined with the local sky-estimation error. The variance map includes both read-out and Poisson noise terms (Crill et al. 2025; Akeson et al. 2025). Since this does not take into account the uncertainty of the fluxes of field objects, it should be regarded as a lower limit; however, it should be close to the true value when sidereal object contamination within the aperture is small.

¹⁹ An 11-inch reflecting telescope manufactured by Celestron LLC

²⁰ IAU observatory code G80, $37^{\circ}4'13.39''$ N, $119^{\circ}24'45.72''$ W

²¹ Manufactured by FLI Kepler, a 4k by 4k CMOS Back Illuminated (BI) camera

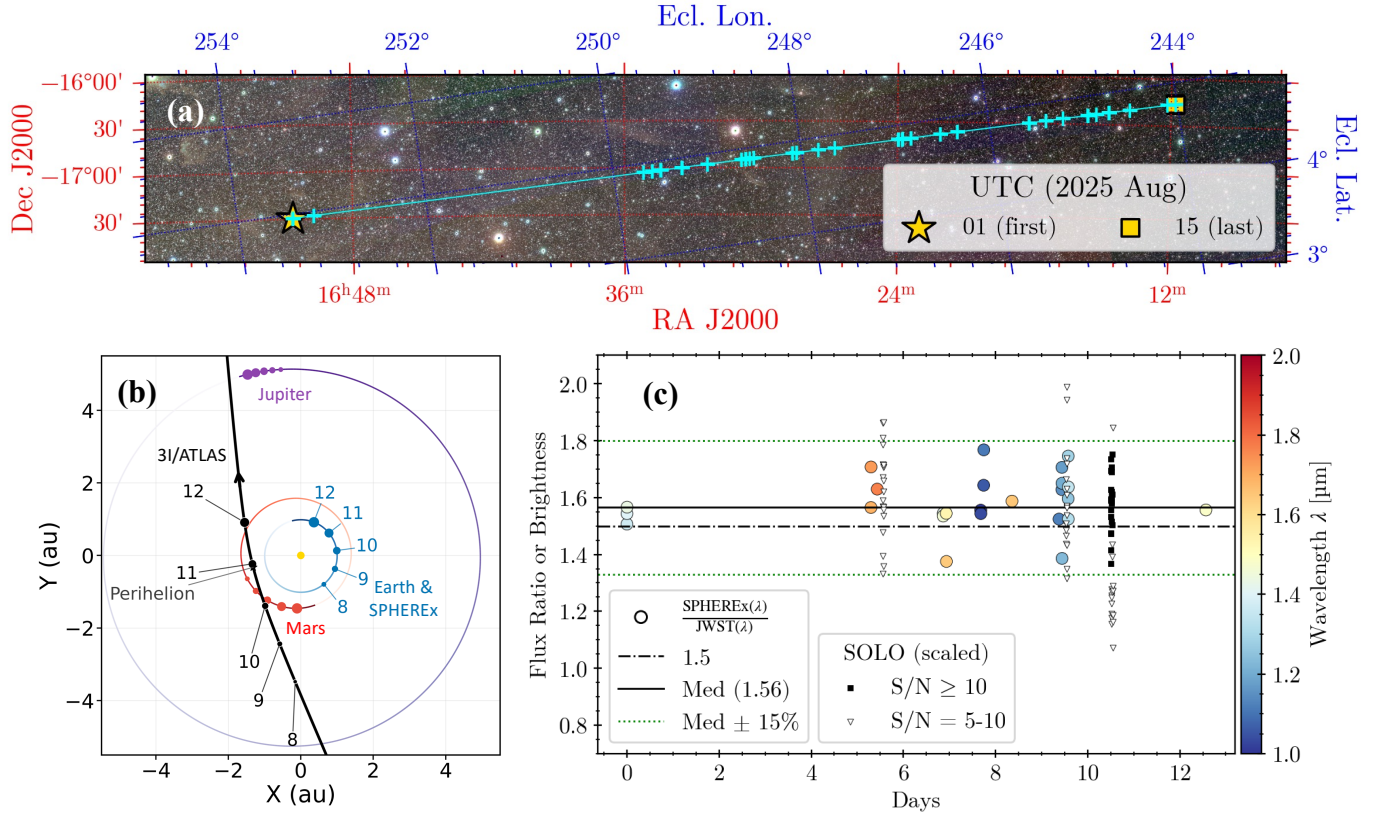


Figure 1. Motion of 3I. **(a)** Color composite from SPHEREx data at 1.185, 1.716, and 2.194 μm for red, green, and blue, respectively. The trajectory of 3I is overlotted, with observed positions marked by crosses. The starting and ending points of our dataset are indicated separately (see legend). **(b)** Orbital motion of 3I (black) projected onto the ecliptic plane. The orbits of Earth, Mars, and Jupiter are shown in blue, red, and purple, respectively. Numbers indicate the positions of the bodies at the first day of each month. 3I’s retrograde motion and perihelion are marked with arrows. **(c)** Lightcurve of 3I produced by taking all $\lambda = 1.0\text{--}1.8\ \mu\text{m}$ SPHEREx flux measurements and dividing them by the JWST flux (Fig. 2b; Cordiner et al. 2025) to leave only lightcurve variations. Also included are SOLO clear-filter brightness measurements scaled to match their median to that of the SPHEREx/JWST ratio. The resulting lightcurve amplitude is within $\pm 15\%$, so the derived reflectance should be correct to within this range considering any lightcurve modulation effects.

We define the contamination factor as

$$F_{\text{field}} \equiv F_{\text{sim}}/F_{2b}. \quad (1)$$

For example, if a contaminant contributes half the flux of 3I, then we expect $F_{\text{field}} = 0.5/(1 + 0.5) \approx 0.3$. The higher this number, the larger the measurement uncertainty.

Among the 160 exposures, 9 were flagged as “a” and are completely discarded because at least one unrecoverable pixel (cold, hot, non-functional, early transient, and early overflow) is within the aperture, and it is unlikely that they can ever be improved. Flag “b” is given to 59, and they are regarded as less reliable as of writing because of strong background source contamination expected and/or calibration ($F_{\text{field}} > 30\%$, object is on the edge of detectors, etc). Finally, 11 were flagged “c”, which means we see a non-negligible contamination likely from background objects identified by visual inspection, that is, the flux interpolated from the refer-

ence catalog does not fully represent the sidereal sources near 3I. In principle, fluxes from exposures with flags “b” and “c” could be improved once SPHEREx obtains images of the same sky regions at the same wavelengths, when suitable “reference” images will be available for subtraction.

4. RESULTS

The direct observables produced by SPHEREx spectrophotometric imaging of 3I in early August 2025 fall into 3 broad categories: temporal lightcurves, spectrophotometry, and imaging.

4.1. Lightcurves

Lightcurve analysis of 3I’s temporal behavior (Fig. 1) shows very little variability of $\lesssim 15\%$ from hours to days timescales, which is also confirmed by independent SOLO observations. This upper limit of variation is also consistent with previous reports (Seligman et al. 2025;

Kareta et al. 2025; Beniyama 2025). The fortuitous lack of temporal variability, explained by an object with a small, likely dark nucleus surrounded by a very bright and high surface area coma (see Section 4.6 below), meant that we could quickly cull out any background contaminated images and proceed straight to analysis of the data.

4.2. Spectra

The measured fluxes of 3I are scaled to the geometry of $r_{\text{obs}} = r_{\text{hel}} = 1$ au assuming $F_{\lambda} \propto r_{\text{hel}}^{-2} r_{\text{obs}}^{-2}$ (Fig. 2a). The reflectance spectrum is derived by dividing the SPHEREx measurements by the solar flux. We can break up the spectrum into 5 main regions: the 0.7–1.5 μm scattered light region; the 1.5–2.3 μm mixed organics plus water absorption region; the 2.4–3.3 μm water ice absorption region; the 3.2–3.7 μm organics absorption region; and the 3.7–5.0 μm mixed region. Superimposed on top of the continua are weak gas emission features due to H₂O at 2.7–2.8 μm and CO at 4.6–4.8 μm , and a strong CO₂ emission feature at 4.2–4.4 μm . The CO₂ feature is strong enough that we believe we have detected not only normal ¹²CO₂ centered in a doublet at 4.25 and 4.27 μm , but also a small side shoulder due to ¹³CO₂ centered at 4.31 μm . The agreement in spectral shape with the JWST spectrum of Cordiner et al. (2025) taken in one visit during the middle of our observational window is excellent; the main disagreement between the two spectral datasets is in the amplitude of the gas emission lines, with SPHEREx’s consistently being higher due to the much larger effective aperture of its measurements compared to the 3'' \times 3'' FOV of the JWST NIRSPEC IFU (approximately 1/4 the area of one SPHEREx pixel).

Because the CO₂ coma is definitely extended beyond 1' (Fig. 3), the nominal aperture photometry will give only a lower limit of the flux. Integrating the total flux using the radial profile is discussed below.

4.3. Gas Production Rates

We adopt a production rate Q_{gas} via

$$Q_{\text{gas}} = 2\pi v_{\text{gas}} \rho N_{\text{gas}} \quad (2)$$

where N_{gas} is the average column density of the gas within a circular aperture of projected radius ρ on the sky, centered on the nucleus, and where v_{gas} is the gas emission velocity. We use $v_{\text{gas}} = (0.85 \text{ km/s})/\sqrt{r_{\text{hel}}}$ in au = 0.48 km/s (Cochran et al. 2012) and $r = 11,600$ km here. The average column density is given by (cf. e.g. Konno & Wyckoff 1989)

$$N_{\text{gas}} = \frac{4r_{\text{obs}}^2 F_{\nu} \Delta\lambda}{\rho^2 g h \lambda} \left(\frac{r_{\text{hel}}}{1 \text{ au}} \right)^2 \quad (3)$$

where F_{ν} is the average flux density (i.e. power per area per frequency bandwidth) in the band from the gas; $r_{\text{hel}} = 3.2$ au and $r_{\text{obs}} = 2.6$ au are the heliocentric and observer-centric distances to 3I, respectively; g is the fluorescence efficiency at 1 au for the emission band in question, and we use $g = 2.9 \times 10^{-4}$, 2.6×10^{-3} , and 2.6×10^{-4} photons per second per molecule for H₂O 2.85 μm , CO₂ 4.25 μm , and CO 4.7 μm emission bands, respectively (Crovisier et al. 1997); h is Planck’s constant; $\Delta\lambda$ is the bandwidth for the narrow-band assumption, and we use 0.08 μm for H₂O and 0.037 μm for all others; and λ is the wavelength of the band.

Given the SPHEREx H₂O, ¹²CO₂, ¹³CO₂, and CO gas emission fluxes of 58, 8610, 70, and 59 mJy measured in 2 pixel radius effective apertures and corrected for 3I’s relative position to $r_{\text{hel}} = 1$ au, $r_{\text{obs}} = 1$ au (Fig. 2), we derive gas production rates of $Q_{\text{H}_2\text{O}} = 3.2 \times 10^{26}$ molec/sec \pm 20%, $Q_{^{12}\text{CO}_2} = 1.6 \times 10^{27}$ molec/sec \pm 10%, $Q_{^{13}\text{CO}_2} = 1.3 \times 10^{25}$ molec/sec \pm 25%, and $Q_{\text{CO}} = 1.0 \times 10^{26}$ molec/sec \pm 25%. The rates of CO₂ and H₂O emission are consistent with the activity of in-bound thermally processed short-period Solar System comets at 3.2 au (Harrington Pinto et al. 2022), where water gas emission is “not fully on yet”, and the ratio of $Q_{^{13}\text{CO}_2}/Q_{^{12}\text{CO}_2} \sim 1/100$ is consistent with the ISM value of 70, although the CO production rate at $< 0.1 Q_{\text{CO}_2}$ is very low (see Discussion section). These updated Q_{gas} values are also consistent with the preliminary values reported for the first 70 visits by Lisse et al. (2025), and by Cordiner et al. (2025) from their JWST observations of 06-Aug-2025 UT taken roughly halfway through the SPHEREx observing run.

4.4. Images

We extracted cutout images at the specified wavelengths, with the few pixels flagged as cold, hot, non-functional, or otherwise erroneously masked. The masked images were then median-combined, and the background removed by subtracting the smoothed 10 by 50 pixels rectangular regions, centered at 75 pixels away to the left and right of the center of 3I. The resulting stacked, background removed SPHEREx near-infrared images of 3I are shown in Fig. 3.

Images at different wavelength ranges probe the distribution of dust and important spectral features by molecules (Sect. 4.2). The large extension seen in ¹²CO₂ versus H₂O is not surprising given the orders of magnitude higher measured flux emission from CO₂ gas, the object’s location well within the ~ 12 au CO₂ ice line of the solar system, and the long lifetime (~ 6 days) vs photolysis and SWCX compared to water (~ 1 day). However, the falloff of the CO₂ coma with respect to

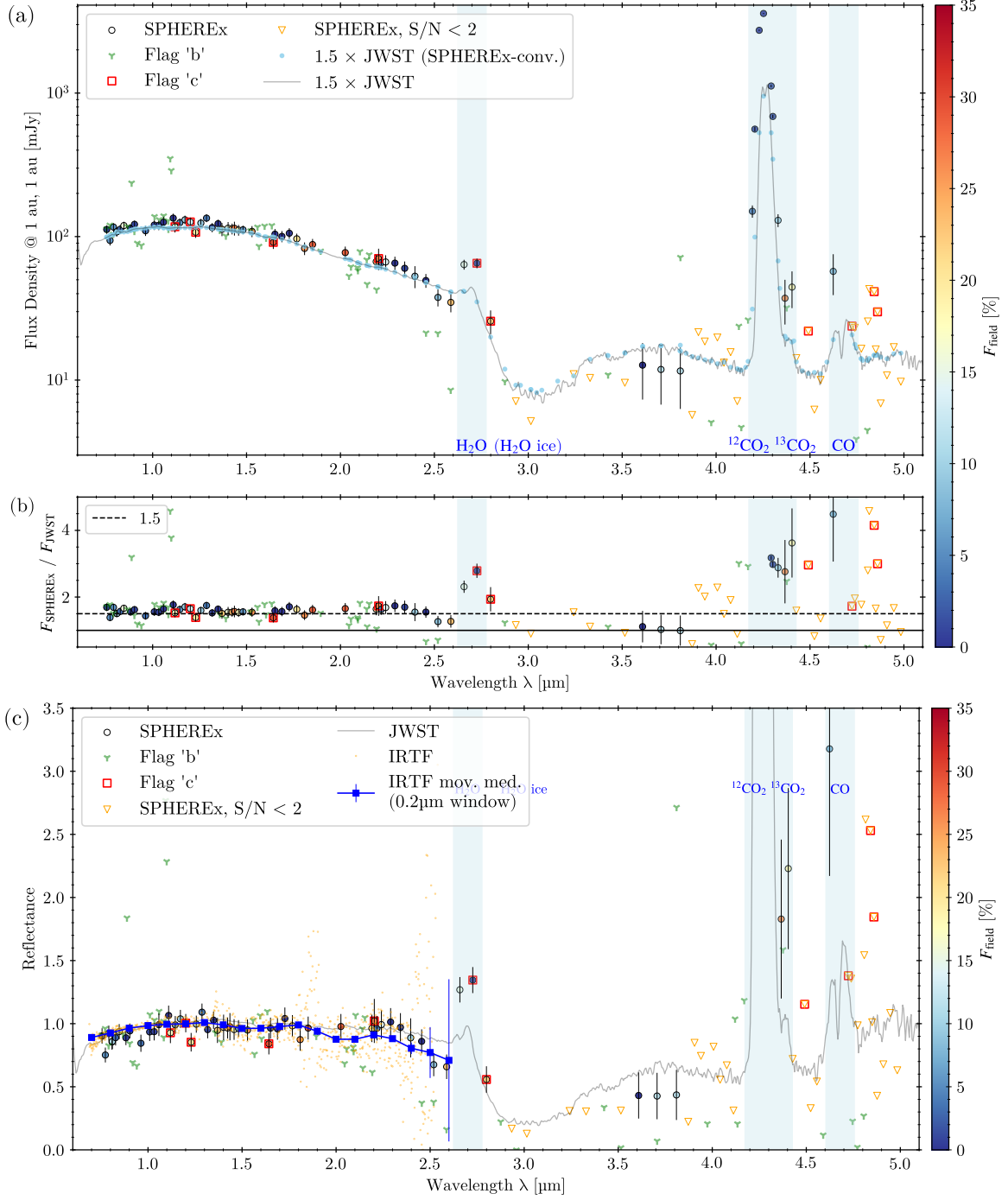


Figure 2. (a) The flux density of the measurements, scaled to the geometry of $r_{\text{obs}} = r_{\text{hel}} = 1$ au. The JWST measurements (Cordiner et al. 2025) are scaled by a constant factor of 1.5 to match the SPHEREx measurements. For flags, see Table 1 and text for explanation. The skyblue points are the JWST measurements, convolved with the pixel spectral throughput at the SPHEREx pixel for that observation, using the SPHEREx Sky Simulator (Hui et al. 2024; Crill et al. 2025). Blue shades indicate important spectral features. Colors of “good” measurements indicate F_{field} (Eq. 1). (b) The distance-corrected ratio of the SPHEREx to JWST flux, showing that SPHEREx measurements are systematically higher than JWST. This indicates the spatial extendedness of the object, 3l. The error-bars are not shown for $S/N < 2$ data. (c) The reflectance, normalized at $1.2 \mu\text{m}$ for SPHEREx, JWST, and the IRTF measurements. The blue line shows the moving median of the IRTF data with a $0.2 \mu\text{m}$ window.

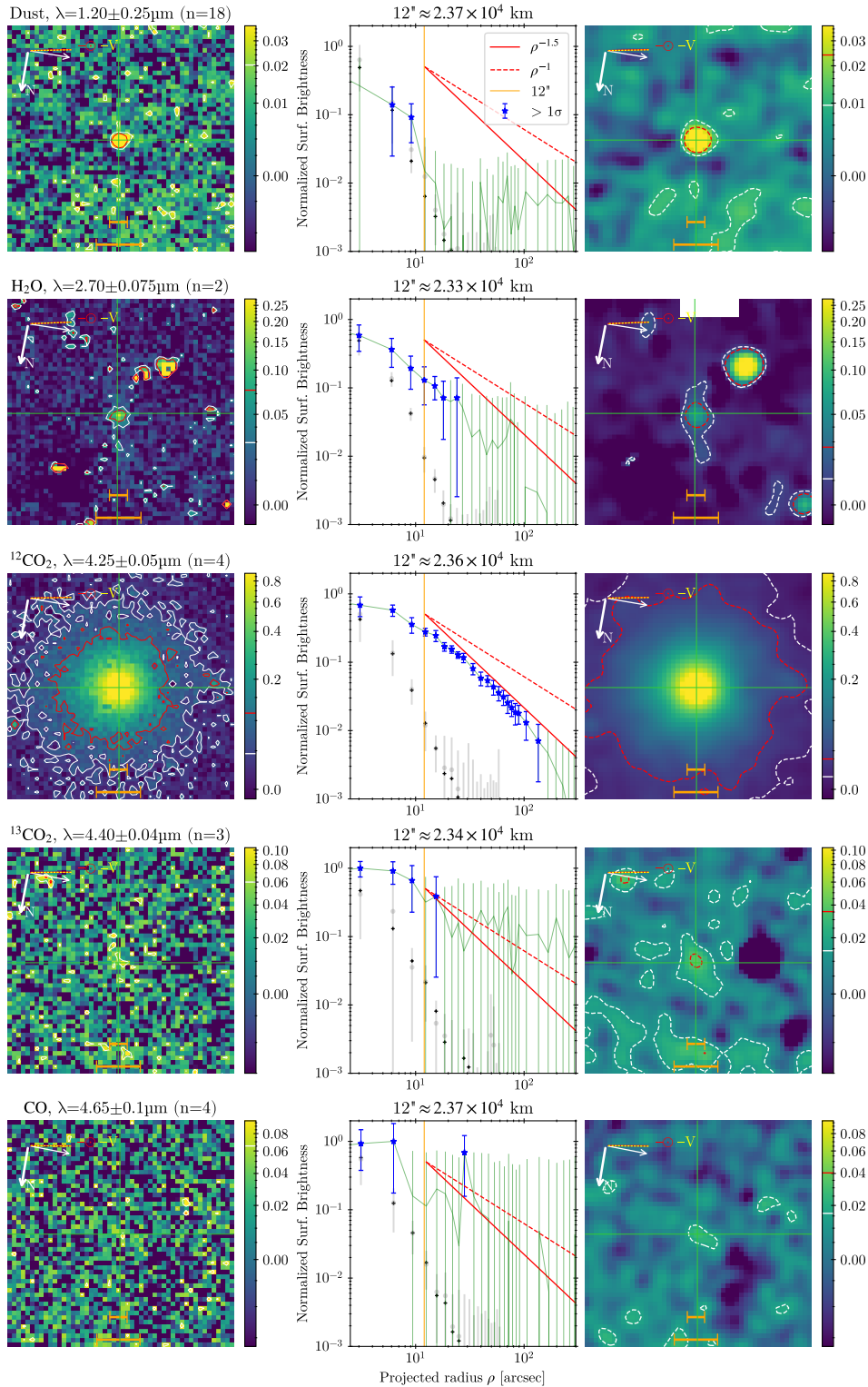


Figure 3. Median combined images ($\approx 5' \times 5'$) and radial profiles. **Left column:** The stacked images, after simulation and background subtractions, in MJy/sr unit (see scale bars). The orange bars at the bottom indicate aperture diameter ($24''$) and $1'$. **Middle column:** The radial profile of 3I in the stacked image (green; blue if the signal is above the $1\text{-}\sigma$ scatter), mean (gray) and median (black) of 30 brightest field stars within $\lesssim 10'$, respectively. Each profile is normalized to the central pixel. The red solid and dashed lines are for $\rho^{-1.5}$ and ρ^{-1} profiles, respectively, for the radius ρ . The nominal aperture radius (orange vertical lines) and corresponding length at 3I (title) are shown. **Right column:** Same as the left column but convolved with a standard deviation of 1.5-pixel gaussian filter for visualization. In the left and right columns, celestial North (white thick arrow), East (white thin arrow), anti-solar (red solid) and anti-velocity (yellow dashed) vectors are shown in the top left corner. The white and red contours (also shown in the color bar to the right of each panel) are 2- and 5- σ above the background, respectively.

projected radial distance ρ is definitely steeper than $1/\rho$, implying that there is either acceleration of the outflow occurring or there is destruction of the outflowing CO_2 going on.

The lack of a bright water gas coma is puzzling as 3I was not far outside the Solar system’s “water ice line” at $r_{\text{hel}} = 2.5$ au during the observations. We are led to conclude that 3I was emitting large chunks of mixed $\text{CO}_2 + \text{H}_2\text{O}$ ice into its coma at the time of observation, and that evaporative cooling of CO_2 was pinning the chunks’ temperature at ~ 120 K and greatly suppressing the H_2O ice’s vapor pressure (Lisse et al. 2021). A corollary of this argument is that once 3I comes well within the water ice line of the solar system at 2.5 au, its outgassing behavior will markedly change and increase as majority matrix water ice itself starts evaporating rapidly. This will destroy many of the large chunks of ice in the coma, changing it over to a small particle dominated cloud with a more anti-solar pointing tail, while driving the sublimation front inward towards the nucleus.

4.5. Radial profiles

Azimuthally averaged radial profiles for each stacked image were constructed by taking the modal value of 1-pixel-thick circular annuli after $3\text{-}\sigma$ clipping (Bertin & Arnouts 1996). Resulting observed radial profiles representative of dust, H_2O , $^{12}\text{CO}_2$, $^{13}\text{CO}_2$, and CO , are shown in (Fig. 3). The profiles were then compared to those found for nearby stars in the SPHEREx all-sky survey, for determination if 3I appeared extended versus a point source. If so, we further compared them to the canonical $1/\rho$ behavior expected for a nucleus emitting material at constant velocity into a 4π sphere (A’Hearn & Festou 1990).

Only at wavelengths characteristic of emission from H_2O and $^{12}\text{CO}_2$ do we see significant extension above stellar; the profile for H_2O is noisy enough that we cannot say much more about its power-law slope. By contrast, the $^{12}\text{CO}_2$ profile slope is very well defined, and clearly falls off more quickly than a ρ^{-1} coma, more like a $\rho^{-3/2}$ coma. Assuming that the CO_2 coma is optically thin, (valid for the observed $Q_{\text{CO}_2} = 1 \times 10^{27}$ emission rate into $r \lesssim 6''$) this is indicative of either significant photolytic + charge exchange destruction of the CO_2 , or significant acceleration of the CO_2 . Given that the CO_2 coma extends out to $\sim 3' = 384,000$ km at 3.2 au, and CO_2 gas molecules with a photolytic lifetime of ~ 6 days = 526,000 s must move at an average speed of 0.7 km/sec, it is hard to see how many of them could be getting destroyed close to the nucleus. Instead they are likely accelerating due to significant pressure

in the gas releasing coma, an explanation supported by noting that the (Cochran et al. 2012) gas velocity relation has the molecules emitted thermally at 0.48 km/sec (Section 4.3), and that the CO_2 coma gas profiles of Fig. 3 appear quite flat for the first $\sim 15''$ (32,000 km) before bending past a sublimation front to follow a $\rho^{-3/2}$ trend at larger distances.

4.6. Nucleus Size

Since the scattered light signal from 3I is unresolved spatially versus a point source by SPHEREx, we analyze its importance by taking limiting cases. Firstly, if we assume all the flux were to originate as sunlight scattered off of a nuclear surface of geometric albedo $p_V = 0.04$ at the phase angles $\alpha = 16.3\text{--}17.2^\circ$ of 3I during the observation, we find an effective spherical radius of the object of ~ 23 km (Lisse et al. 2025). However, we know this assumption is patently false, as Hubble Space Telescope observations of the object have placed a firm upper limit, after fitting and tracing the coma flux back to the central PSF pixels, of no more than an 2.5 km radius, $p_V = 0.04$ point source residual. Further, no significant lightcurve has ever been measured for 3I, and a large asymmetric rotating nucleus, as all comets observed to date have shown, will produce significant lightcurve variations. And finally, the giant CO_2 coma mapped by SPHEREx shows a flat-topped structure within $15''$ (2.5 pixels or 32,000 km) of the nucleus.

The solution to all these issues is the same: the presence of a small, rotating, dark nucleus surrounded by a stable, approximately 100 times brighter coma. (Cometary comae are typically static in brightness over hours to days unless the nucleus produces a huge outburst of emission or has a bright focused region of jet-like activity on its surface). Solar system comets where the nucleus is greatly outshone by its coma are rare but not unheard of; they are the handful of small, “hyperactive” comets like 41P/Wirtanen and 103P/Hartley 2 (103P, hereafter) with so much icy dust in their comae that the coma solid material has more surface area than the nucleus and out-produces the nucleus in gas emission. These comets thus require high amounts of large, long lived icy particle emission, and further appear to be CO_2 gas dominated ((Lisse et al. 2009); see the Discussion Section for further arguments for the connection between 3I and 103P). This was just the kind of behavior 3I was exhibiting during the early August 2025 SPHEREx observations reported here.

5. DISCUSSION

All of the observations reported here (the giant CO_2 coma, the lack of any observed lightcurve variability,

the prevalence of large coma grains, and the 100 times greater coma scattered light flux than a 2.5 km radius, 0.04 geometric albedo spherical object would produce) are consistent with an object spectrally dominated by bright, CO₂- and water ice-rich coma material. The low amount of H₂O gas production observed by SPHEREx in August 2025 can be explained by the object’s having only recently arrived from the cold depths of interstellar space and its remoteness from the Sun (outside the water ice line between 3.4 and 3.1 au) during the observational period (Lisse et al. 2021, 2022a). The lack of strong CO emission is slightly surprising, as the CO-ice line in the solar system lies at ~ 40 au from the Sun, until one realizes it is an indication of hypervolatile depletion.

Given the current turbulent mix of information currently posted on 3I it is important to state that there are known, studied natural solar system comets producing analogous behavior. A strong predominance of CO₂ gas emission coupled with CO hypervolatile depletion has been seen in solar system hyperactive comets like 103P (A’Hearn et al. 2012, $Q_{\text{CO}_2}/Q_{\text{H}_2\text{O}} \sim 20\%$; $Q_{\text{CO}}/Q_{\text{H}_2\text{O}} \sim 0.15\%$) and 46P/Wirtanen (McKay et al. 2021, $Q_{\text{CO}_2}/Q_{\text{H}_2\text{O}} \sim 15\%$; $Q_{\text{CO}}/Q_{\text{H}_2\text{O}} < 0.5\%$). In fact, 103P is the comet with the lowest known ratio of CO to CO₂ (Harrington Pinto et al. 2022, see Fig. 4a). Hyperactive comets are defined as comets with gas production rates many times what sublimation from their nucleus surfaces can/should be able to support; their gas production is instead produced primarily from large, long-lived icy grains emitted into the surrounding coma by the nucleus.

The connection between 3I and 103P is bolstered by reports of 3I’s abundant C2 and CN emission, putting it akin to the spectral Class A comets of Fink 2009’s spectral survey, which also contains hyperactive comets 103P and 46P/Wirtanen. Further, comparison of the inbound visible lightcurve vs heliocentric distance for the 103P 2010 apparition to the current inbound lightcurve vs distance for 3I (Fig. 4b) shows an excellent match (Figure 4a).

103P was especially well studied during the close (~ 1000 km minimum distance) flyby of the NASA Deep Impact Extended mission (A’Hearn et al. 2011, in November 2010), which imaged large chunks of CO₂ rich material being ejected “in a reverse snow” from one of the comet’s lobes and measured a coma $\sim 5\times$ brighter than the nucleus in total scattered light flux (Figure 4c). The large chunks of CO₂-rich material are explained as primordial remnants of solid CO₂ ice which have lost much of their more hypervolatile ice phases (e.g., CO, N₂, and CH₄). The imaging results from the Deep Impact extended mission suggest that the regions of its nu-

cleus emitting CO₂-rich ice are separated from regions producing water gas, and the source ices may be physically separated.

5.1. Physical Behavior Hypotheses

There are several hypotheses that have been proposed to explain 3I’s physical behavior. For example, it has been proposed that 3I originated in a very CO-poor but CO₂-rich exosystem (i.e., the “nature hypothesis” to the following “evolutionary nurture proposals”). Assuming that the CO : CO₂ ratio is directly reflective of the natal system’s C:O abundance ratio (c.f., Bodewits et al. 2020), we find this explanation problematic, as this would imply a system with a host star C/O ratio $< 1/10$ the Sun’s, and a dearth of reduced aliphatic and aromatic species as well. $[\text{C}/\text{Fe}]$ and $[\text{C}/\text{H}] < -1.0$ for a nearby Milky Way star is highly improbable (Hinkel et al. 2017; Lisse et al. 2017; Mészáros et al. 2025), and the aliphatic and PAH absorption features for 3I in the JWST NIRSPEC spectrum of Cordiner et al. (2025) look to be of reasonably normal strength.

Another hypothesis from the August 2025 observations suggests that 3I is in the same state of advanced thermal processing, mass loss, and age as analogously behaving 103P. Because of 103P’s very small size but moderate to high gas production rate, coupled with its lack of hypervolatile CO and presence of large CO₂ -rich grains, it has been argued that it has been highly thermally processed by the Sun over hundreds to thousands of orbits, and is near the end of its life (Lisse et al. 2009). To get to this state, it has lost much of its original mass, so that its current surface used to be its core material, buried under kilometer’s worth of cometary material at its creation.

Another possibility is that we are observing a comet-like body from an exosystem with near-solar composition, but also a body with unusual alteration of its surface layers by Gyrs of continual galactic cosmic ray and stellar XUV irradiation kept at $T_{\text{galactic ISR}} = 15\text{--}30$ K (Zhu & Huang 2014). This would produce an CO : CO₂ number ratio of ≈ 0.1 if the surface material started out as H₂O : CO₂ ice only, without any starting CO (Maggiolo et al. 2025). However, if CO was initially present in the newly ejected comet’s surface at typical primordial-like abundance ratios of CO : CO₂ = 0.5–10, the irradiated result should have a final CO : CO₂ ratio ~ 1 (Moore 1991). The observed SPHEREx CO : CO₂ ratio of 0.06 ± 0.03 is consistent with a predicted value of 0.1 for a starting pure H₂O : CO₂ ice case, and the large emitted dust grains are reminiscent of the mantle grains emitted from surface processed short-period solar system comets (Lisse 2002) implying that 3I was thermally

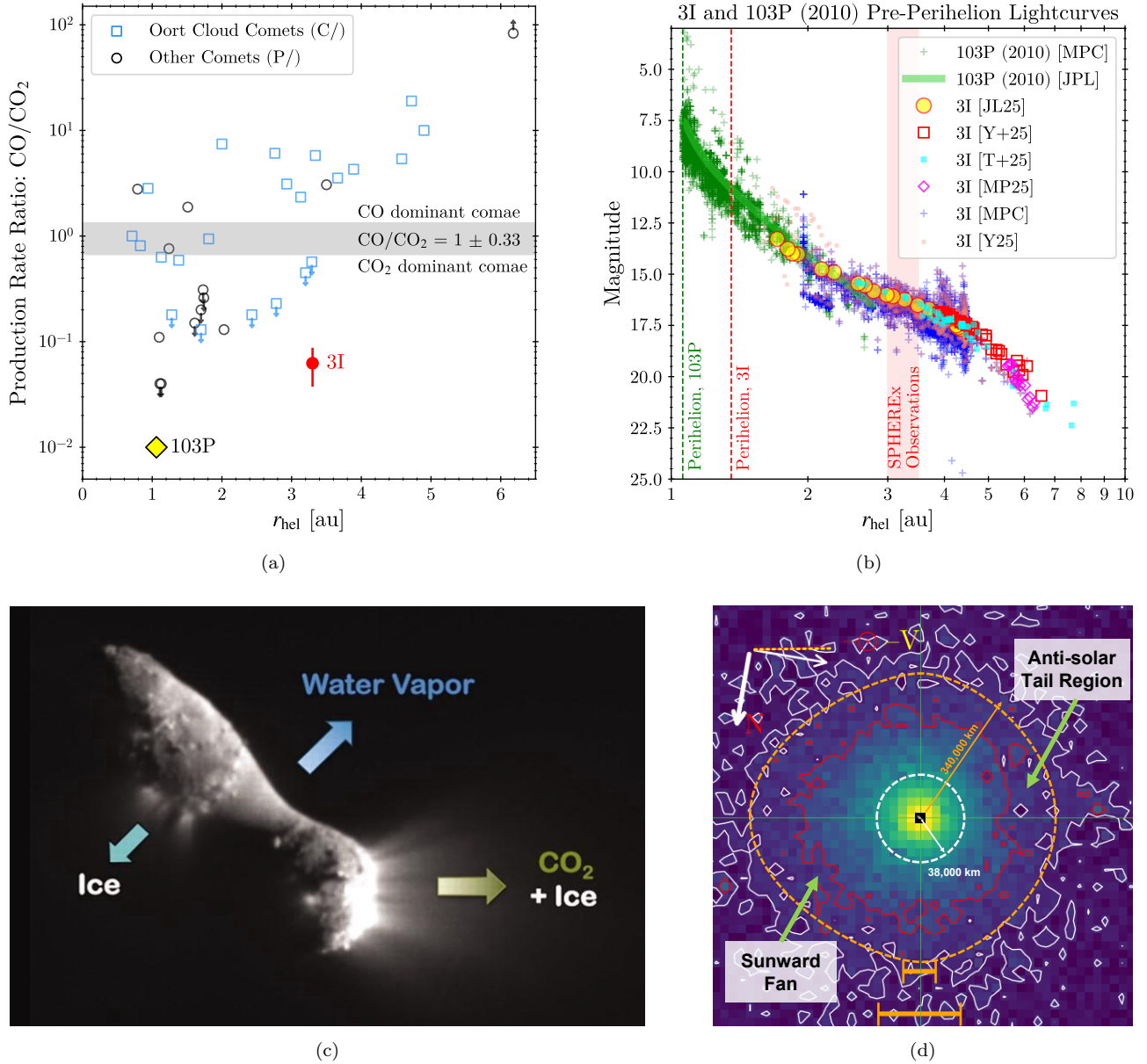


Figure 4. (a) CO/CO₂ gas production rate ratios of solar system comets (Harrington Pinto et al. 2022). The CO or CO₂ dominance criteria of 1 ± 0.33 is indicated as horizontal shadow (Harrington Pinto et al. 2022). The ratio of 3I makes it extremely CO poor and equivalent to the most thermally processed comet in the 2022 survey, 103P. (b) Pre-perihelion optical lightcurves observed for comet 103P during the 2010–2011 apparition and 3I in May - Oct 2025. Published data from (Jewitt & Luu 2025; Tonry et al. 2025; Ye et al. 2025) have been shifted to match the absolute magnitude of Minor Planet Center (MPC) Database^a, the T-mag from JPL Horizons ephemerides service^b, and the data kindly shared by S. Yoshida (2025^c, priv. comm.). There is very good agreement between the two inbound lightcurve trends. An inherent spread of ~ 0.5 mag in the measurements between nights and between observers can be seen. (c) Close flyby imaging of the $\sim 1.5 \times 0.6 \times 0.6$ km comet 103P nucleus as obtained by the Deep Impact Extended mission (A’Hearn et al. 2011). A marked bilobate nuclear morphology was seen, with unusually large (mm to dm) chunks of CO₂ rich ice and gas emanating from the end of the smaller lobe and the middle of the larger lobe. The surrounding coma, filled with large long lived icy grains, was found to be at least 5 times brighter and more actively emitting gas than the nucleus. While the nucleus of 3I has never been resolved, given its similar behavior, it could possibly share similar morphological characteristics. (d) Schematic of the 3I object derived from SPHEREx CO₂ photometric mapping. The < 2.5 km radius nucleus (Jewitt et al. 2025) was not resolved at the SPHEREx pixel scale of $6.15'' \approx 11,600$ km at 2.6 au distance, but a notional nucleus image has been included at the origin to give the reader its location and a sense of scale. Two distances have been marked off: The $\sim 38,000$ km (white dashed circle) inside of which we think coma ice is actively sourcing CO₂ by sublimation; and $\sim 340,000$ km (orange dashed oval), the minimum radial distance to which we detect CO₂ gas at 2- σ level.

^ahttps://www.minorplanetcenter.net/db_search/show_object?object_id=3I for 3I and https://www.minorplanetcenter.net/db_search/show_object?object_id=103P for 103P.

^b<https://ssd.jpl.nasa.gov/horizons/app.html>

^c<http://www.aerith.net/comet/catalog/0003I/2025N1.html>

processed enough in its home system to severely deplete hypervolatiles in its near-surface layers before ejection and irradiation.

The way to distinguish between the [Complete thermal CO depletion of an object] versus [Surface CO thermal depletion followed by meters worth of galactic radiation treatment] hypotheses is to search for a marked change in the relative CO emission behavior of 3I both in increased abundance and direct nuclear emission morphology, as it passes close to the Sun on 30 Oct 2025 and its interior regions, beneath its ~ 10 m surface irradiation processed zone (Maggiolo et al. 2025), become heated.

5.2. ISO Evolution and Home System Implications

A strongly thermally processed state for 3I has important implications. By analogy to 103P’s behavior, it tells us that 3I has undergone 100s to 1,000s of close passages by its natal host/birth star (we reject the possibility that 3I has undergone hundreds to thousands of close passages of random galactic stars on its passage to the solar system; this rate of close passage for a single object, even one as old as the galaxy, would imply a huge rate of interstellar object passages & detections in our solar system, which is not seen).

These close thermally altering passages could have been accomplished either as a primordial body formed in-place near its birth system’s CO₂ ice line (to ensure minimal CO but extensive labile CO₂ ice incorporation) and quickly ejected soon after PPD disk clearing, or, as seen currently in our own mature system, as an ice-rich KBO that became scattered into its inner system for a few hundred near-star orbits before ejection.

Finally we end with a piece of scholarly speculation. Naive models of ISO creation would suggest the maximal number of ISOs created by a system should be when it hosts the most free-flying small planetesimals that are dynamically hot. I.e., when the system is very young, within the first few Myrs of the host stars formation. But this is also the era when a system’s protoplanetary disk is optically thick near its midplane and planetesimals in the densest part of the disk remain cold and thermally unprocessed. PPDs are seen to clear within 5–10 Myrs of host star formation though (Rieke et al. 2005; Ben et al. 2025, and references therein), and the first heavy thermal processing of KBOs estimated to occur in 1–40 Myrs (Davidsson 2021; Steckloff et al. 2021; Lisse et al. 2021, 2022b; Parhi & Prrialnik 2023).

Planetary migration and Oort Cloud formation involving small body ejection processes can take 100’s of Myrs to complete (Brasser & Morbedeli 2013; Garrod 2019). We can thus plausibly argue that PPDs can

clear and small body thermal evolutionary processes can occur more rapidly than dynamical processes can cool down and mature in a system, and we should see a mix of volatile rich, hypervolatile depleted, and totally devolatilized ejected objects as our ISOs. This is precisely what we have seen so far in highly-devolatilized 1I/Oumuamua, hypervolatile-rich 2I/Borisov, and well-thermally processed 3I.

6. CONCLUSIONS AND FUTURE WORK

In conclusion, the SPHEREx spacecraft observed ISO 3I from 01 to 15-Aug-2025 UT using 102 band, $R = 40$ –130 spectrophotometry. Photometric imagery, spectroscopy, and light curves of the ISO were obtained. From these, robust detections of slightly extended water gas emission at 2.7–2.8 μm and highly extended ¹²CO₂ gas at 4.23–4.27 μm were found. More tentative detections of ¹³CO₂ and CO gas were seen. A slightly extended coma of H₂O was detected, and a huge surrounding atmosphere of CO₂ extending out to at least 3’ was discovered. No jets were detected in the coma imagery, but a slight sunward pointing asymmetry was seen in the CO₂ coma. Derived gas production rates for the 4 species were $Q_{\text{H}_2\text{O}} = 3.2 \times 10^{26} \pm 20\%$, $Q_{^{12}\text{CO}_2} = 1.6 \times 10^{27} \pm 10\%$, $Q_{^{13}\text{CO}_2} = 1.3 \times 10^{25} \pm 25\%$, and $Q_{\text{CO}} = 1.0 \times 10^{26} \pm 25\%$.

Registration and co-adding of dozens of scattered light continuum images at 1.0–1.5 μm produced a high S/N ratio image consistent with a stellar point source of no extension. The same images were used to create a lightcurve, for which variability $\lesssim 15\%$ was seen from beginning to end of the observing period. The absolute brightness of 3I at 1.0–1.5 μm is consistent with a nucleus of effective radius $R_{\text{nuc}} \lesssim 2.5$ km, as reported by HST (Jewitt et al. 2025) surrounded by a 100 times brighter coma. The SPHEREx spectral continuum measured over 2 weeks is highly consistent with the continuum reported by JWST during its single visit to the object on 06 Aug 2025 (Cordiner et al. 2025). The 1.5–4.0 μm continuum structure shows a strong feature commensurate with water ice + refractory organics absorption. The overall shape of this reflectance continuum is very similar to that reported for the cliff-type KBOs by (Pinilla-Alonso 2025)

The August SPHEREx observations provided the first detection of strong CO₂ emission from the comet into a giant extended surrounding coma, proving that CO₂ sublimation from large icy coma grains is the main driver for the observed outgassing activity and explaining its extended morphology as the product of CO₂ gas sublimation that was undetectable in the first reported UVIS characterizations of the object. The moderate observed

water gas production rate can be explained as an object just coming in from the cold depths of interstellar space that was observed at $r_{\text{hel}} = 3.2$ au from the Sun outside the water ice line.

In many ways the observed activity behavior of 3I, including its preponderance of CO₂ emission, lack of CO output, small size, and predominance of large chunks of water-ice rich icy material in a flux-dominant coma is reminiscent of the behavior of short period comet 103P, target of the NASA Deep Impact extended mission in 2010 and a “hyperactive comet” (A’Hearn et al. 2011; Lisse et al. 2009). Such an object could have undergone hundreds to thousands of close perihelion passages by its natal birth star inside the system’s water ice line, as 103P has by our Sun. Whether this was due to 3I forming within a few au of its birth star or being scattered into this region after formation but before ejection is not clear.

Compared to the naïve expectation that solar systems shed the majority of their comets in their first few Myrs of existence when their small icy planetesimals are most abundant, most hypervolatile ice rich, and most dynamically hot, so that all ISOs should be like 2I/Borisov, this suggests that ISOs are thermally processed quicker than they dynamically relax. This hypothesis needs to be tested by population studies of many more ISOs than the 3 currently known, and hopefully many more will be studied by the SPHEREx mission’s all-sky survey.

ACKNOWLEDGMENTS

This paper relies on data obtained by the SPHEREx Observatory (operated by Caltech and JPL on behalf of the National Aeronautics Space Administration under contract 80GSFC18C0011) that is hosted by IPAC as part of the IRSA archive (10.26131/IRSA652 SPHEREx Quick Release Spectral Images - QR2). We are indebted to the SPHEREx project for obtaining additional pointings at 3I, approximately 100 percent more, than their nominal survey would have obtained less than 3 months after the start of the survey by testing and implementing a new commanding protocol. We have also used optical lightcurve trending data kindly supplied by S. Yoshida. The research was carried out at the Jet Propulsion Laboratory, California Institute of Technology, the Johns Hopkins Applied Physics Laboratory, and Arizona State University under a contract with the National Aeronautics and Space Administration (80NM0018D0004). The authors also acknowledge the Texas Advanced Computing Center (TACC) ²² at The University of Texas at Austin for providing computational resources that have contributed to the research results reported within this paper.

AUTHOR CONTRIBUTIONS

All listed authors contributed importantly to the creation and production of this manuscript.

Facilities: SPHEREx, IRTF, SOLO

Software: SPHEREx-Sky-Simulator (Crill et al. 2025), spiceypy (Annex et al. 2020), SPICE (Acton et al. 2018; Acton 1996), kete (Dahlen et al. 2025), skyloc²³, SPHEREx-SSO, astropy (Astropy Collaboration et al. 2013, 2018, 2022), ccdproc (Craig et al. 2025), photutils (Bradley et al. 2025),

APPENDIX

A. APPENDIX INFORMATION

REFERENCES

- Acton, C., Bachman, N., Semenov, B., & Wright, E. 2018, Planet. Space Sci., 150, 9, doi: [10.1016/j.pss.2017.02.013](https://doi.org/10.1016/j.pss.2017.02.013)
- Acton, C. H. 1996, Planet. Space Sci., 44, 65, doi: [10.1016/0032-0633\(95\)00107-7](https://doi.org/10.1016/0032-0633(95)00107-7)
- A’Hearn, M. F., & Festou, M. C. 1990, in Physics and Chemistry of Comets, ed. W. F. Huebner, 69–110
- A’Hearn, M. F., Belton, M. J. S., Delamere, W. A., et al. 2011, Science, 332, 1396, doi: [10.1126/science.1204054](https://doi.org/10.1126/science.1204054)
- A’Hearn, M. F., Feaga, L. M., Keller, H. U., et al. 2012, ApJ, 758, 29, doi: [10.1088/0004-637X/758/1/29](https://doi.org/10.1088/0004-637X/758/1/29)

²² <http://www.tacc.utexas.edu>

²³ <https://github.com/ysBach/skyloc>

- Akeson, R., Dubois-Felsmann, G., Faisst, A., et al. 2025, SPHEREX Explanatory Supplement, Tech. rep., Caltech/IPAC, Jet Propulsion Laboratory. https://irsa.ipac.caltech.edu/data/SPHEREx/docs/SPHEREx_Expsupp_QR_v1.3.pdf
- Annex, A., Pearson, B., Seignovert, B., et al. 2020, *The Journal of Open Source Software*, 5, 2050, doi: [10.21105/joss.02050](https://doi.org/10.21105/joss.02050)
- Astropy Collaboration, Robitaille, T. P., Tollerud, E. J., et al. 2013, *A&A*, 558, A33, doi: [10.1051/0004-6361/201322068](https://doi.org/10.1051/0004-6361/201322068)
- Astropy Collaboration, Price-Whelan, A. M., Sipőcz, B. M., et al. 2018, *AJ*, 156, 123, doi: [10.3847/1538-3881/aabc4f](https://doi.org/10.3847/1538-3881/aabc4f)
- Astropy Collaboration, Price-Whelan, A. M., Lim, P. L., et al. 2022, *ApJ*, 935, 167, doi: [10.3847/1538-4357/ac7c74](https://doi.org/10.3847/1538-4357/ac7c74)
- Ben, G. M., Jose, J., & Hernández, J. 2025, *MNRAS*, 541, 2246, doi: [10.1093/mnras/staf1089](https://doi.org/10.1093/mnras/staf1089)
- Beniyama, J. 2025, *PASJ*, 77, L71, doi: [10.1093/pasj/psaf097](https://doi.org/10.1093/pasj/psaf097)
- Bertin, E., & Arnouts, S. 1996, *A&AS*, 117, 393, doi: [10.1051/aas:1996164](https://doi.org/10.1051/aas:1996164)
- Bock, J. J., Aboobaker, A. M., Adamo, J., et al. 2025, arXiv e-prints, arXiv:2511.02985, doi: [10.48550/arXiv.2511.02985](https://doi.org/10.48550/arXiv.2511.02985)
- Bodewits, D., Noonan, J., & Feldman, P. e. a. 2020, *Natureastro*, 4, 867, doi: [10.1038/s41550-020-1095-2](https://doi.org/10.1038/s41550-020-1095-2)
- Bradley, L., Sipőcz, B., Robitaille, T., et al. 2025, *astropy/photutils: 2.2.0*, Zenodo, doi: [10.5281/zenodo.596036](https://doi.org/10.5281/zenodo.596036)
- Brasser, R., & Morbedeli, A. 2013, *Icarus*, 225, 40, doi: [10.1016/j.icarus.2013.03.012](https://doi.org/10.1016/j.icarus.2013.03.012)
- Bryan, S., Bock, J., Burk, T., et al. 2025, arXiv e-prints, arXiv:2508.20332, doi: [10.48550/arXiv.2508.20332](https://doi.org/10.48550/arXiv.2508.20332)
- Chandler, C. O., Bernardinelli, P. H., Jurić, M., et al. 2025, arXiv e-prints, arXiv:2507.13409, doi: [10.48550/arXiv.2507.13409](https://doi.org/10.48550/arXiv.2507.13409)
- Cochran, A. L., Barker, E. S., & Gray, C. L. 2012, *Icarus*, 218, 144, doi: [10.1016/j.icarus.2011.12.010](https://doi.org/10.1016/j.icarus.2011.12.010)
- Cordiner, M. A., Roth, N. X., Kelley, M. S. P., et al. 2025, *ApJL*, 991, L43, doi: [10.3847/2041-8213/ae0647](https://doi.org/10.3847/2041-8213/ae0647)
- Craig, M., Crawford, S., Seifert, M., et al. 2025, *astropy/ccdproc: 2.5.1*: The final 2.x release, 2.5.1, Zenodo, doi: [10.5281/zenodo.593516](https://doi.org/10.5281/zenodo.593516)
- Crill, B. P., Bach, Y. P., Bryan, S. A., et al. 2025, *ApJS*, 281, 10, doi: [10.3847/1538-4365/ae04cc](https://doi.org/10.3847/1538-4365/ae04cc)
- Crovisier, J., Leech, K., Bockelee-Morvan, D., et al. 1997, *Science*, 275, 1904, doi: [10.1126/science.275.5308.1904](https://doi.org/10.1126/science.275.5308.1904)
- Dahlen, D., Kwon, Y. G., Masiero, J. R., Spahr, T., & Mainzer, A. K. 2025, arXiv e-prints, arXiv:2509.04666, doi: [10.48550/arXiv.2509.04666](https://doi.org/10.48550/arXiv.2509.04666)
- Davidsson, B. J. R. 2021, *MNRAS*, 505, 5654, doi: [10.1093/mnras/stab1593](https://doi.org/10.1093/mnras/stab1593)
- Denneau, L., Siverd, R., Tonry, J., et al. 2025, *Minor Planet Electronic Circulars*, 2025-N12, doi: [10.48377/MPEC/2025-N12](https://doi.org/10.48377/MPEC/2025-N12)
- Doré, O., Werner, M. W., Ashby, M., et al. 2016, arXiv e-prints, arXiv:1606.07039, doi: [10.48550/arXiv.1606.07039](https://doi.org/10.48550/arXiv.1606.07039)
- Doré, O., Werner, M. W., Ashby, M. L. N., et al. 2018, arXiv e-prints, arXiv:1805.05489, doi: [10.48550/arXiv.1805.05489](https://doi.org/10.48550/arXiv.1805.05489)
- Garrod, R. 2019, *ApJ*, 884, 32, doi: [10.3847/1538-4357/ab418e](https://doi.org/10.3847/1538-4357/ab418e)
- Harrington Pinto, O., Womack, M., Fernandez, Y., & Bauer, J. 2022, *PSJ*, 3, 247, doi: [10.3847/PSJ/ac960d](https://doi.org/10.3847/PSJ/ac960d)
- Hinkel, N. R., Mamajek, E. E., Turnbull, M. C., et al. 2017, *ApJ*, 848, 34, doi: [10.3847/1538-4357/aa8b0f](https://doi.org/10.3847/1538-4357/aa8b0f)
- Hui, H., Korngut, P. M., Condon, S., et al. 2024, in *Society of Photo-Optical Instrumentation Engineers (SPIE) Conference Series*, Vol. 13092, *Space Telescopes and Instrumentation 2024: Optical, Infrared, and Millimeter Wave*, ed. L. E. Coyle, S. Matsuura, & M. D. Perrin, 130923N, doi: [10.1117/12.3018463](https://doi.org/10.1117/12.3018463)
- Jewitt, D., Hui, M.-T., Mutchler, M., Kim, Y., & Agarwal, J. 2025, *ApJL*, 990, L2, doi: [10.3847/2041-8213/adf8d8](https://doi.org/10.3847/2041-8213/adf8d8)
- Jewitt, D., & Luu, J. 2025, *ApJL*, 994, L3, doi: [10.3847/2041-8213/ae1832](https://doi.org/10.3847/2041-8213/ae1832)
- Kareta, T., Champagne, C., McClure, L., et al. 2025, *ApJL*, 990, L65, doi: [10.3847/2041-8213/adfbdf](https://doi.org/10.3847/2041-8213/adfbdf)
- Konno, I., & Wyckoff, S. 1989, *Advances in Space Research*, 9, 163, doi: [10.1016/0273-1177\(89\)90256-1](https://doi.org/10.1016/0273-1177(89)90256-1)
- Lisse, C. 2002, *Earth Moon and Planets*, 90, 497, doi: [10.1023/A:1021519408600](https://doi.org/10.1023/A:1021519408600)
- Lisse, C. M., Sitko, M. L., Marengo, M., Kane, S. R., & Desch, S. 2017, in *LPI Contributions*, Vol. 2042, *Habitable Worlds 2017: A System Science Workshop*, ed. LPI Editorial Board, 4061
- Lisse, C. M., Fernandez, Y. R., Reach, W. T., et al. 2009, *PASP*, 121, 968, doi: [10.1086/605546](https://doi.org/10.1086/605546)
- Lisse, C. M., Young, L. A., Cruikshank, D. P., et al. 2021, *Icarus*, 356, 114072, doi: [10.1016/j.icarus.2020.114072](https://doi.org/10.1016/j.icarus.2020.114072)
- Lisse, C. M., Gladstone, G. R., Young, L. A., et al. 2022a, *PSJ*, 3, 112, doi: [10.3847/PSJ/ac6097](https://doi.org/10.3847/PSJ/ac6097)
- Lisse, C. M., Steckloff, J. K., Prialnik, D., et al. 2022b, *PSJ*, 3, 251, doi: [10.3847/PSJ/ac9468](https://doi.org/10.3847/PSJ/ac9468)
- Lisse, C. M., Bach, Y. P., Bryan, S., et al. 2025, *Research Notes of the American Astronomical Society*, 9, 242, doi: [10.3847/2515-5172/ae0293](https://doi.org/10.3847/2515-5172/ae0293)

- Maggiolo, R., Dhooghe, F., Gronoff, G., de Keyser, J., & Cessateur, G. 2025, arXiv e-prints, arXiv:2510.26308, doi: [10.48550/arXiv.2510.26308](https://doi.org/10.48550/arXiv.2510.26308)
- McKay, A. J., DiSanti, M. A., Cochran, A. L., et al. 2021, PSJ, 2, 21, doi: [10.3847/PSJ/abd71d](https://doi.org/10.3847/PSJ/abd71d)
- Mészáros, S., Jofré, P., Johnson, J. A., et al. 2025, AJ, 170, 96, doi: [10.3847/1538-3881/ade4b9](https://doi.org/10.3847/1538-3881/ade4b9)
- Parhi, A., & Prialnik, D. 2023, MNRAS, 522, 2081, doi: [10.1093/mnras/stad1086](https://doi.org/10.1093/mnras/stad1086)
- Pinilla-Alonso, N. 2025, Natureastro, 9, 620, doi: [10.1038/s41550-024-02433-2](https://doi.org/10.1038/s41550-024-02433-2)
- Rieke, G. H., Su, K. Y. L., Stansberry, J. A., et al. 2005, ApJ, 620, 1010, doi: [10.1086/426937](https://doi.org/10.1086/426937)
- Seligman, D. Z., Micheli, M., Farnocchia, D., et al. 2025, ApJL, 989, L36, doi: [10.3847/2041-8213/adf49a](https://doi.org/10.3847/2041-8213/adf49a)
- Steckloff, J. K., Lisse, C. M., Safrit, T. K., et al. 2021, Icarus, 356, 113998, doi: [10.1016/j.icarus.2020.113998](https://doi.org/10.1016/j.icarus.2020.113998)
- Tonry, J., Denneau, L., Alarcon, M., et al. 2025, arXiv e-prints, arXiv:2509.05562, doi: [10.48550/arXiv.2509.05562](https://doi.org/10.48550/arXiv.2509.05562)
- Ye, Q., Kelley, M. S. P., Hsieh, H. H., et al. 2025, ApJL, 993, L31, doi: [10.3847/2041-8213/ae147b](https://doi.org/10.3847/2041-8213/ae147b)
- Zhu, J., & Huang, M. 2014, A&A, 564, 5, doi: [10.1051/0004-6361/201322723](https://doi.org/10.1051/0004-6361/201322723)

Table 1. Observation log

ObsID	λ	Mid JD	Flag	F_λ	dF_λ	r_{hel}	r_{obs}	α	$F_{\lambda,1}$	Refl	F_{field}
	μm	UTC		mJy	mJy	au	au	$^\circ$	mJy		
2025W33_1B_0134_1	0.7543	2460899.2257	b	1.5806	0.1298	3.146	2.689	17.89	113.0997	0.9117	0.66
2025W33_1B_0576_1	0.7555	2460901.6032		1.6693	0.1128	3.070	2.669	18.70	112.0514	0.9028	0.00
2025W33_1B_0134_2	0.7720	2460899.2272	b	1.6806	0.1290	3.146	2.689	17.89	120.2481	0.9617	0.68
2025W33_1B_0576_2	0.7732	2460901.6047		1.4010	0.1102	3.070	2.669	18.70	94.0379	0.7516	0.05
2025W33_1B_0134_3	0.7904	2460899.2286	b	1.4530	0.1281	3.146	2.689	17.89	103.9565	0.8258	0.72
2025W33_1B_0576_3	0.7914	2460901.6062		1.7357	0.1133	3.070	2.669	18.70	116.4995	0.9247	0.05
2025W33_1B_0183_1	0.8086	2460899.4981		1.5183	0.1098	3.137	2.686	17.98	107.8433	0.8554	0.03
2025W33_1B_0576_4	0.8102	2460901.6077		1.6141	0.1113	3.070	2.669	18.70	108.3380	0.8588	0.11
2025W33_1B_0183_2	0.8277	2460899.4996		1.5842	0.1100	3.137	2.686	17.98	112.5217	0.8892	0.03
2025W33_1B_0183_3	0.8469	2460899.5011		1.6796	0.1074	3.137	2.686	17.98	119.2890	0.9370	0.16
2025W33_1B_0183_4	0.8669	2460899.5026	b	1.6537	0.1115	3.137	2.686	17.99	117.4487	0.9180	0.34
2025W33_1B_0447_1	0.8825	2460900.9246		1.6678	0.1088	3.092	2.674	18.47	114.0067	0.8880	0.01
2025W33_2C_0073_1	0.8880	2460902.2831	b	3.5835	0.1330	3.049	2.663	18.92	236.2225	1.8377	0.33
2025W33_2C_0255_1	0.9028	2460903.0304	b	1.6838	0.1201	3.025	2.657	19.16	108.8071	0.8427	0.57
2025W33_1B_0447_2	0.9034	2460900.9261		1.7800	0.1116	3.092	2.674	18.47	121.6712	0.9423	0.01
2025W33_2C_0220_1	0.9105	2460902.8942	a	1.6894	0.1147	3.029	2.658	19.12	109.5633	0.8453	0.31
2025W32_2D_0224_1	0.9184	2460896.2371	b	1.1585	0.1155	3.242	2.718	16.81	89.9130	0.6914	0.34
2025W32_2D_0224_2	0.9402	2460896.2386	b	1.1165	0.1183	3.242	2.718	16.81	86.6476	0.6660	0.37
2025W32_2D_0343_1	0.9621	2460896.8510		1.4387	0.1157	3.222	2.711	17.04	109.7945	0.8448	0.03
2025W32_2D_0343_2	0.9851	2460896.8525	a	1.4547	0.1163	3.222	2.711	17.04	111.0136	0.8573	0.03
2025W32_2D_0343_3	1.0087	2460896.8540		1.5769	0.1212	3.222	2.711	17.04	120.3376	0.9347	0.01
2025W33_1B_0642_1	1.0100	2460901.9458	b	2.0724	0.1201	3.059	2.666	18.81	137.8480	1.0715	0.42
2025W32_2D_0343_4	1.0326	2460896.8555		1.5691	0.1165	3.222	2.711	17.04	119.7352	0.9367	0.01
2025W33_1B_0642_2	1.0341	2460901.9473	b	1.9734	0.1268	3.059	2.666	18.81	131.2523	1.0273	0.57
2025W32_2D_0355_1	1.0578	2460896.9169		1.6547	0.1500	3.220	2.711	17.06	126.0554	0.9919	-0.00
2025W33_1B_0642_3	1.0587	2460901.9488	b	2.0959	0.2123	3.059	2.666	18.81	139.3993	1.0975	0.63
2025W32_2D_0355_2	1.0830	2460896.9184	b	1.6904	0.2139	3.220	2.711	17.06	128.7693	1.0183	-0.04
2025W33_1B_0642_4	1.0839	2460901.9503	b	1.6923	0.2425	3.059	2.666	18.81	112.5511	0.8901	0.66
2025W33_1B_0010_3	1.0937	2460898.5514	b	4.7982	0.8953	3.168	2.695	17.65	349.6425	2.7681	-0.07
2025W32_2D_0213_4	1.0992	2460896.1734	b	3.7113	0.3139	3.244	2.718	16.79	288.5384	2.2846	0.86
2025W32_2D_0355_3	1.1095	2460896.9199		1.7655	0.1303	3.220	2.711	17.06	134.4829	1.0649	-0.01
2025W33_1B_0010_4	1.1190	2460898.5529	c	1.6069	0.1423	3.167	2.695	17.65	117.0914	0.9278	0.17
2025W33_1B_0020_1	1.1448	2460898.6147		1.7179	0.1216	3.166	2.694	17.67	124.9685	0.9902	0.06
2025W33_1B_0020_2	1.1722	2460898.6162		1.7996	0.1239	3.165	2.694	17.67	130.9044	1.0379	0.10
2025W33_1B_0020_3	1.2005	2460898.6177	c	1.7384	0.1259	3.165	2.694	17.68	126.4498	1.0040	0.13
2025W33_1B_0020_4	1.2291	2460898.6192	c	1.4737	0.1273	3.165	2.694	17.68	107.1920	0.8529	0.20
2025W33_1B_0049_1	1.2567	2460898.7511		1.7138	0.1163	3.161	2.693	17.72	124.2077	0.9960	0.09
2025W33_1B_0049_2	1.2869	2460898.7526		1.8549	0.1162	3.161	2.693	17.72	134.4296	1.0909	0.04

Table 1 *continued*

Table 1 (continued)

ObsID	λ	Mid JD	Flag	F_λ	dF_λ	r_{hel}	r_{obs}	α	$F_{\lambda,1}$	Refl	F_{field}
	μm	UTC		mJy	mJy	au	au	$^\circ$	mJy		
2025W33_1B_0049_3	1.3170	2460898.7541		1.5957	0.1165	3.161	2.693	17.72	115.6397	0.9529	0.01
2025W33_1B_0049_4	1.3483	2460898.7556		1.6960	0.1143	3.161	2.693	17.72	122.9079	1.0275	-0.02
2025W32_2D_0189_1	1.3574	2460896.0344	b	1.4183	0.1227	3.248	2.720	16.74	110.6876	0.9284	0.32
2025W31_2A_0219_1	1.3691	2460889.1740		1.1899	0.1253	3.470	2.802	14.08	112.4649	0.9467	0.22
2025W32_2D_0189_2	1.3899	2460896.0359	b	1.2936	0.1253	3.248	2.720	16.74	100.9479	0.8545	0.35
2025W31_2A_0219_2	1.4018	2460889.1755		1.2101	0.1256	3.470	2.802	14.08	114.3738	0.9708	0.16
2025W32_2D_0189_3	1.4229	2460896.0374		1.4522	0.1255	3.248	2.720	16.74	113.3258	0.9657	0.23
2025W31_2A_0219_3	1.4354	2460889.1770		1.2089	0.1339	3.470	2.802	14.08	114.2550	0.9758	0.27
2025W32_2D_0189_4	1.4576	2460896.0389		1.4229	0.1225	3.248	2.720	16.74	111.0323	0.9536	0.17
2025W33_1B_0599_1	1.4811	2460901.7420		1.6676	0.1148	3.066	2.667	18.74	111.5249	0.9619	0.06
2025W33_1B_0399_1	1.5216	2460900.6541	b	1.5960	0.1209	3.100	2.676	18.38	109.8950	0.9569	0.43
2025W32_2D_0201_1	1.5290	2460896.1047		1.3956	0.1240	3.246	2.719	16.76	108.7057	0.9490	0.26
2025W33_1B_0399_2	1.5583	2460900.6556	b	1.6922	0.1288	3.100	2.676	18.38	116.5121	1.0267	0.35
2025W32_2D_0201_2	1.5663	2460896.1062	b	1.0992	0.1233	3.246	2.719	16.77	85.6153	0.7579	0.37
2025W33_1B_0399_3	1.5961	2460900.6571	b	1.7193	0.1282	3.100	2.676	18.38	118.3695	1.0636	0.37
2025W32_2D_0201_3	1.6041	2460896.1077	b	1.2537	0.1192	3.246	2.719	16.77	97.6421	0.8809	0.33
2025W33_1B_0399_4	1.6346	2460900.6586	b	1.7319	0.1178	3.100	2.676	18.38	119.2337	1.0961	0.35
2025W32_2D_0201_4	1.6425	2460896.1092	c	1.1699	0.1173	3.246	2.719	16.77	91.1135	0.8406	0.29
2025W32_2D_0480_4	1.6513	2460897.5324		1.3873	0.1205	3.200	2.705	17.29	103.9303	0.9644	-0.00
2025W32_1A_0612_1	1.6882	2460894.4706		1.2311	0.1104	3.299	2.736	16.15	100.3018	0.9585	-0.07
2025W32_1A_0612_2	1.7276	2460894.4721		1.2954	0.1092	3.298	2.736	16.15	105.5386	1.0405	0.00
2025W32_1A_0637_1	1.7675	2460894.6067		1.1888	0.1024	3.294	2.735	16.20	96.4935	0.9830	0.20
2025W32_1A_0637_2	1.8089	2460894.6082		1.0186	0.1030	3.294	2.735	16.20	82.6736	0.8736	0.26
2025W32_1A_0637_3	1.8514	2460894.6097		1.0842	0.1022	3.294	2.735	16.20	87.9947	0.9651	0.28
2025W32_1A_0637_4	1.8946	2460894.6112	b	0.9764	0.1063	3.294	2.735	16.21	79.2467	0.9003	0.34
2025W32_2D_0426_4	2.0255	2460897.2641		1.0247	0.1041	3.209	2.707	17.19	77.3232	0.9774	0.28
2025W32_2D_0017_1	2.0455	2460895.0837	b	0.6625	0.0992	3.279	2.730	16.38	53.0690	0.6838	0.41
2025W31_2A_0156_1	2.0559	2460888.8341	b	0.6445	0.1313	3.481	2.807	13.94	61.5102	0.8001	0.75
2025W32_1A_0662_1	2.0912	2460894.7445	b	0.7503	0.0914	3.290	2.733	16.26	60.6676	0.8144	0.38
2025W32_2D_0017_2	2.0930	2460895.0852	b	0.7243	0.0919	3.279	2.730	16.38	58.0158	0.7800	0.30
2025W31_2A_0156_2	2.1037	2460888.8356	b	0.8240	0.1328	3.481	2.807	13.94	78.6373	1.0654	0.52
2025W32_1A_0662_2	2.1400	2460894.7460	b	0.8510	0.0910	3.290	2.733	16.26	68.8102	0.9590	0.32
2025W32_2D_0017_3	2.1421	2460895.0867	b	0.5806	0.0939	3.279	2.730	16.38	46.5038	0.6486	0.38
2025W31_2A_0156_3	2.1531	2460888.8371	b	0.7823	0.1243	3.481	2.807	13.94	74.6552	1.0468	0.36
2025W32_1A_0662_3	2.1903	2460894.7475		0.8273	0.0932	3.290	2.733	16.26	66.8928	0.9626	0.18
2025W32_2D_0017_4	2.1923	2460895.0882	b	0.5322	0.0913	3.279	2.730	16.39	42.6302	0.6144	0.40
2025W31_2A_0156_4	2.2031	2460888.8386	c	0.7369	0.1258	3.481	2.806	13.94	70.3206	1.0215	0.27
2025W33_1B_0499_1	2.2173	2460901.1996		0.9691	0.0979	3.083	2.672	18.56	65.7561	0.9640	0.04
2025W32_1A_0662_4	2.2408	2460894.7490		0.8229	0.0939	3.290	2.733	16.26	66.5343	0.9923	0.14
2025W32_2D_0091_2	2.2899	2460895.4945		0.8248	0.0898	3.266	2.725	16.54	65.3319	1.0132	-0.01

Table 1 continued

Table 1 (continued)

ObsID	λ	Mid JD	Flag	F_λ	dF_λ	r_{hel}	r_{obs}	α	$F_{\lambda,1}$	Refl	F_{field}
	μm	UTC		mJy	mJy	au	au	$^\circ$	mJy		
2025W32_2D_0091_3	2.3421	2460895.4960		0.7588	0.0879	3.266	2.725	16.54	60.1004	0.9709	0.01
2025W32_2D_0091_4	2.3965	2460895.4975		0.6686	0.1167	3.265	2.725	16.54	52.9495	0.8874	0.10
2025W33_1B_0576_1	2.4549	2460901.6032		0.7359	0.0815	3.070	2.669	18.70	49.4018	0.8600	-0.03
2025W33_1B_0134_1	2.4555	2460899.2257	b	0.2977	0.0957	3.146	2.689	17.89	21.3013	0.3708	0.90
2025W33_1B_0134_2	2.5188	2460899.2272	b	0.2957	0.0841	3.146	2.689	17.89	21.1555	0.3789	0.91
2025W33_1B_0576_2	2.5191	2460901.6047		0.5614	0.0760	3.070	2.669	18.70	37.6839	0.6749	0.09
2025W33_1B_0134_3	2.5870	2460899.2286	b	0.1190	0.0819	3.146	2.689	17.89	8.5140	0.1611	0.96
2025W33_1B_0576_3	2.5878	2460901.6062		0.5184	0.0765	3.070	2.669	18.70	34.7952	0.6585	0.23
2025W33_1B_0183_1	2.6546	2460899.4981	a	0.6898	0.0695	3.137	2.686	17.98	48.9947	0.9734	-0.02
2025W33_1B_0576_4	2.6581	2460901.6077		0.9513	0.0755	3.070	2.669	18.70	63.8524	1.2686	0.15
2025W33_1B_0183_2	2.7266	2460899.4996	c	0.9177	0.0704	3.137	2.686	17.98	65.1836	1.3454	-0.00
2025W33_1B_0183_3	2.7994	2460899.5011	c	0.3622	0.0683	3.137	2.686	17.98	25.7283	0.5574	0.22
2025W33_1B_0183_4	2.8755	2460899.5026	b	0.1377	0.0653	3.137	2.686	17.99	9.7773	0.2224	0.68
2025W33_1B_0447_1	2.9337	2460900.9246		0.1042	0.0659	3.092	2.674	18.47	7.1250	0.1678	0.21
2025W33_2C_0073_1	2.9586	2460902.2831	b	-0.0007	0.0773	3.049	2.663	18.92	-0.0490	-0.0012	1.00
2025W33_2C_0255_1	3.0131	2460903.0304	b	-0.1549	0.0672	3.025	2.657	19.16	-10.0110	-0.2476	1.18
2025W33_1B_0447_2	3.0141	2460900.9261		0.0758	0.0646	3.092	2.674	18.47	5.1789	0.1281	0.14
2025W33_2C_0220_1	3.0445	2460902.8942	b	-0.1782	0.0687	3.029	2.658	19.12	-11.5603	-0.2894	1.36
2025W32_2D_0224_1	3.0721	2460896.2371	b	-0.4158	0.0657	3.242	2.718	16.81	-32.2688	-0.8275	4.59
2025W32_2D_0224_2	3.1568	2460896.2386	b	-0.3980	0.0673	3.242	2.718	16.81	-30.8892	-0.8276	3.08
2025W32_2D_0343_1	3.2415	2460896.8510		0.1442	0.1579	3.222	2.711	17.04	11.0012	0.3082	-1.83
2025W32_2D_0343_2	3.3290	2460896.8525		0.1357	0.1407	3.222	2.711	17.04	10.3565	0.3044	-0.19
2025W32_2D_0343_3	3.4221	2460896.8540	a	-0.0930	0.0888	3.222	2.711	17.04	-7.0998	-0.2197	0.07
2025W33_1B_0642_1	3.4250	2460901.9458	b	0.1635	0.0783	3.059	2.666	18.81	10.8745	0.3365	0.80
2025W32_2D_0343_4	3.5143	2460896.8555		0.1255	0.0797	3.222	2.711	17.04	9.5770	0.3116	-0.22
2025W33_1B_0642_2	3.5149	2460901.9473	b	0.0080	0.0739	3.059	2.666	18.81	0.5289	0.0172	0.99
2025W32_2D_0355_1	3.6085	2460896.9169		0.1668	0.0708	3.220	2.711	17.06	12.7099	0.4309	-0.15
2025W33_1B_0642_3	3.6096	2460901.9488	b	-0.0132	0.0703	3.059	2.666	18.81	-0.8747	-0.0297	1.01
2025W32_2D_0355_2	3.7066	2460896.9184		0.1556	0.0671	3.220	2.711	17.06	11.8562	0.4265	0.12
2025W33_1B_0642_4	3.7069	2460901.9503	b	0.0291	0.0696	3.059	2.666	18.81	1.9381	0.0697	0.97
2025W33_1B_0010_3	3.8071	2460898.5514	a	-0.1580	0.1548	3.168	2.695	17.65	-11.5136	-0.4329	-2.09
2025W32_2D_0355_3	3.8096	2460896.9199		0.1520	0.0694	3.220	2.711	17.06	11.5754	0.4352	0.12
2025W32_2D_0213_4	3.8102	2460896.1734	b	0.9210	0.2429	3.244	2.718	16.79	71.5999	2.7140	0.93
2025W33_1B_0010_4	3.8408	2460898.5529	b	-0.4225	0.1487	3.167	2.695	17.65	-30.7858	-1.1774	-2.74
2025W33_1B_0020_1	3.8724	2460898.6147		0.0785	0.1479	3.166	2.694	17.67	5.7124	0.2224	0.15
2025W33_1B_0020_2	3.9059	2460898.6162		0.2967	0.1545	3.165	2.694	17.67	21.5821	0.8482	0.10
2025W33_1B_0020_3	3.9399	2460898.6177		0.2555	0.1502	3.165	2.694	17.68	18.5816	0.7447	0.23
2025W33_1B_0020_4	3.9742	2460898.6192	b	0.0697	0.1523	3.165	2.694	17.68	5.0716	0.2073	0.72
2025W33_1B_0049_1	4.0069	2460898.7511		0.2733	0.1558	3.161	2.693	17.72	19.8053	0.8169	0.07
2025W33_1B_0049_2	4.0418	2460898.7526		0.1826	0.1510	3.161	2.693	17.72	13.2307	0.5556	0.10

Table 1 continued

Table 1 (continued)

ObsID	λ	Mid JD	Flag	F_λ	dF_λ	r_{hel}	r_{obs}	α	$F_{\lambda,1}$	Refl	F_{field}
	μm	UTC		mJy	mJy	au	au	$^\circ$	mJy		
2025W33_1B_0049_3	4.0773	2460898.7541		0.2160	0.1577	3.161	2.693	17.72	15.6519	0.6700	-0.39
2025W33_1B_0049_4	4.1127	2460898.7556		0.0984	0.1606	3.161	2.693	17.72	7.1327	0.3116	-4.41
2025W32_2D_0189_1	4.1213	2460896.0344	b	0.3042	0.1611	3.248	2.720	16.74	23.7420	1.0372	0.32
2025W31_2A_0219_1	4.1342	2460889.1740	b	0.0495	0.1583	3.470	2.802	14.08	4.6787	0.2065	0.77
2025W32_2D_0189_2	4.1572	2460896.0359	a	0.1098	0.1627	3.248	2.720	16.74	8.5657	0.3819	0.57
2025W31_2A_0219_2	4.1703	2460889.1755	b	0.2781	0.1625	3.470	2.802	14.08	26.2830	1.1835	0.27
2025W32_2D_0189_3	4.1931	2460896.0374		1.9231	0.1885	3.248	2.720	16.74	150.0698	6.8255	0.04
2025W31_2A_0219_3	4.2063	2460889.1770		5.9340	0.2253	3.470	2.802	14.08	560.8176	25.5071	0.01
2025W32_2D_0189_4	4.2294	2460896.0389		35.0958	0.3847	3.248	2.720	16.74	2738.6005	125.8045	0.00
2025W33_1B_0599_1	4.2525	2460901.7420		53.6211	0.4486	3.066	2.667	18.74	3586.0773	168.0236	-0.00
2025W33_1B_0399_1	4.2932	2460900.6541		16.2684	0.2982	3.100	2.676	18.38	1120.1553	53.5221	0.02
2025W32_2D_0201_1	4.3022	2460896.1047		8.8229	0.2521	3.246	2.719	16.76	687.2326	32.8367	0.01
2025W33_1B_0399_2	4.3300	2460900.6556		1.8853	0.1940	3.100	2.676	18.38	129.8094	6.3237	0.10
2025W32_2D_0201_2	4.3391	2460896.1062	a	0.5318	0.1862	3.246	2.719	16.77	41.4188	2.0177	0.29
2025W33_1B_0399_3	4.3668	2460900.6571		0.5401	0.1859	3.100	2.676	18.38	37.1844	1.8289	0.26
2025W32_2D_0201_3	4.3762	2460896.1077	b	0.4100	0.1807	3.246	2.719	16.77	31.9365	1.5859	0.36
2025W33_1B_0399_4	4.4042	2460900.6586		0.6458	0.1849	3.100	2.676	18.38	44.4580	2.2288	0.19
2025W32_2D_0201_4	4.4140	2460896.1092	b	-0.2809	0.1862	3.246	2.719	16.77	-21.8757	-1.1072	55.34
2025W32_2D_0480_4	4.4273	2460897.5324		0.1900	0.2175	3.200	2.705	17.29	14.2339	0.7204	-1.09
2025W32_1A_0612_1	4.4591	2460894.4706	a	0.1632	0.2409	3.299	2.736	16.15	13.2932	0.6856	-3.15
2025W32_1A_0612_2	4.4913	2460894.4721	c	0.2695	0.2175	3.298	2.736	16.15	21.9529	1.1536	-0.88
2025W32_1A_0637_1	4.5233	2460894.6067		0.0767	0.2141	3.294	2.735	16.20	6.2241	0.3301	0.24
2025W32_1A_0637_2	4.5564	2460894.6082		0.1235	0.2172	3.294	2.735	16.20	10.0205	0.5414	-0.00
2025W32_1A_0637_3	4.5900	2460894.6097	b	0.0266	0.2223	3.294	2.735	16.20	2.1569	0.1176	0.60
2025W32_1A_0637_4	4.6237	2460894.6112		0.7050	0.2234	3.294	2.735	16.21	57.2192	3.1773	0.08
2025W32_2D_0426_4	4.7235	2460897.2641	c	0.3147	0.2634	3.209	2.707	17.19	23.7504	1.3792	0.02
2025W32_2D_0017_1	4.7389	2460895.0837		0.2891	0.2555	3.279	2.730	16.38	23.1563	1.3567	-0.09
2025W31_2A_0156_1	4.7462	2460888.8341	b	0.0407	0.2621	3.481	2.807	13.94	3.8796	0.2273	0.90
2025W32_1A_0662_1	4.7716	2460894.7445	b	0.0042	0.2547	3.290	2.733	16.26	0.3357	0.0200	0.95
2025W32_2D_0017_2	4.7734	2460895.0852		0.2065	0.2546	3.279	2.730	16.38	16.5452	0.9866	-0.26
2025W31_2A_0156_2	4.7805	2460888.8356	b	-0.0536	0.2696	3.481	2.807	13.94	-5.1183	-0.3052	1.50
2025W32_1A_0662_2	4.8055	2460894.7460	b	0.0553	0.2594	3.290	2.733	16.26	4.4733	0.2691	0.32
2025W32_2D_0017_3	4.8081	2460895.0867		0.3201	0.2670	3.279	2.730	16.38	25.6390	1.5423	-0.03
2025W31_2A_0156_3	4.8153	2460888.8371		0.4519	0.2628	3.481	2.807	13.94	43.1265	2.6168	0.09
2025W32_1A_0662_3	4.8408	2460894.7475	a	-0.0689	0.2663	3.290	2.733	16.26	-5.5716	-0.3410	0.63
2025W32_2D_0017_4	4.8416	2460895.0882	c	0.5161	0.2797	3.279	2.730	16.39	41.3383	2.5301	-0.01
2025W31_2A_0156_4	4.8501	2460888.8386		0.1717	0.2679	3.481	2.806	13.94	16.3823	1.0114	-0.06
2025W33_1B_0499_1	4.8596	2460901.1996	c	0.4405	0.3001	3.083	2.672	18.56	29.8875	1.8451	-0.07
2025W32_1A_0662_4	4.8765	2460894.7490		0.0851	0.2700	3.290	2.733	16.26	6.8800	0.4284	-2.30
2025W32_2D_0091_2	4.9098	2460895.4945		0.1362	0.2893	3.266	2.725	16.54	10.7901	0.6777	6.99

Table 1 continued

Table 1 (*continued*)

ObsID	λ	Mid JD	Flag	F_λ	dF_λ	r_{hel}	r_{obs}	α	$F_{\lambda,1}$	Refl	F_{field}
	μm	UTC		mJy	mJy	au	au	$^\circ$	mJy		
2025W32_2D_0091_3	4.9463	2460895.4960		0.2143	0.3055	3.266	2.725	16.54	16.9733	1.0843	-0.81
2025W32_2D_0091_4	4.9837	2460895.4975		0.1231	0.3297	3.265	2.725	16.54	9.7467	0.6306	-3.60

NOTE—ObsID is the observation ID of SPHEREx (each ID contains 6 frames from 6 arrays). λ is the nominal band center of the pixel where 3I center is located. Mid JD is the midpoint Julian date of the exposure. Flag indicates less reliable data (see text for detailed explanation). F_λ and dF_λ are the flux and uncertainty. r_{hel} and r_{obs} are the helio- and observer-centric distances to 3I, respectively. α is the phase (Sun-target-observer) angle. $F_{\lambda,1}$ is the reduced flux at $r_{\text{hel}} = r_{\text{obs}} = 1$ au assuming $F_\lambda \propto r_{\text{hel}}^{-2} r_{\text{obs}}^{-2}$. Refl is the reflectance normalized to 1 at $1.2 \pm 0.1 \mu\text{m}$. F_{field} is the fractional contamination from background objects relative to the aperture photometry measured on images *before* subtraction of the simulated background within the aperture.